Journal of Materials Chemistry B

ROYAL SOCIETY OF CHEMISTRY

PAPER

View Article Online
View Journal | View Issue

Cite this: J. Mater. Chem. B, 2026, 14, 2630

Laser-induced graphene on the surface of carbon-coated 3D-printed microneedle arrays for minimally invasive electrochemical detection of olanzapine

Sachin Kadian,[a] Siba Sundar Sahoo,[b] Fahad Munshe,[b] Shubhangi Shukla[a] and Roger J. Narayan *[ab]

We have developed a straightforward and scalable fabrication strategy to create laser-induced graphene on the tips of a carbon-coated 3D-printed microneedle array-based wearable electrochemical sensor to detect OZP in interstitial fluid. The device used a 3D-printed customized microneedle array, followed by spray coating of conductive carbon and silver inks to form the working, counter, and reference electrodes. Furthermore, the carbon-coated microneedle array-based working electrode was laser-treated to alter the surface into a graphitic structure for enhanced sensitivity. After physical and electrochemical characterization, the fabricated microneedle sensor was employed for detection of OZP. Under optimized settings, the microneedle sensor exhibited high sensitivity and specificity toward OZP, with a broad linear range of 0.05–500 μM and a lowest limit of detection of 0.0026 μM. The practical applicability was validated by detecting OZP in artificial interstitial fluid while penetrating a skin-like parafilm model and phantom gel matrix, which demonstrated the potential and practicability of the platform for minimally invasive monitoring of antipsychotic drugs. The obtained results highlight the feasibility of this cost-effective, scalable, and minimally invasive microneedle platform for monitoring OZP; this platform can also be readily adapted for the preparation of other wearable biosensors.

Received 24th September 2025,
Accepted 20th January 2026

DOI: 10.1039/d5tb02162f

rsc.li/materials-b

1. Introduction

Schizophrenia is a complex and debilitating psychiatric disorder that is often characterized by profound disruptions in cognition, affects regulation, mood, perception, emotions, and behavior.[1,2] This condition affects approximately 100 million people across the globe; the onset of the condition commonly occurs during late adolescence or early adulthood and often persists as a lifelong condition.[3] Due to its chronic nature, schizophrenia imposes a substantial burden not only on affected individuals and their families, but also on healthcare systems.[2] Consequently, the implementation of comprehensive and effective treatment strategies is critical, not only for symptom reduction and relapse prevention, but also for the restoration of functional capacity.[4,5]

Recently, olanzapine (OZP), a thienobenzodiazepine derivative and a second-generation (atypical) antipsychotic agent, with notable antagonistic activity at dopaminergic (D1–D4), serotonergic (5-HT2A/2C), and adrenergic (α1) receptor subtypes, has been approved by the United States Food and Drug Administration for the pharmacological management of schizophrenia and other psychotic spectrum disorders that are characterized by abnormal neurological function.[6,7] Furthermore, clinical trials have demonstrated that OZP surpasses haloperidol in attenuating both negative and positive symptoms associated with schizophrenia (*e.g.*, avolition, social withdrawal, delusions, hallucinations, and paranoia). Despite its therapeutic advantages, OZP is associated with several adverse metabolic effects (*e.g.*, weight gain, obesity, insulin resistance, dyslipidemia, elevated cholesterol levels, and high triglyceride levels) as well as cardiovascular complications (*e.g.*, arrhythmias, fainting, or sudden cardiac death).[8,9] Additionally, some patients may experience extrapyramidal and neurovegetative side effects (*e.g.*, visual disturbances, postural disturbances, hypersalivation, dysarthria, and psychomotor retardation).[9,10] Furthermore, the interindividual variability in pharmacokinetics and pharmacodynamics necessitates the precise monitoring of drug levels for better management of therapeutic outcomes and management of potential adverse effects.

[a] *Joint Department of Biomedical Engineering, University of North Carolina and North Carolina State University, Raleigh, NC, 27695, USA. E-mail: rjnaraya@ncsu.edu, skadian@ncsu.edu*
[b] *Department of Materials Science and Engineering, North Carolina State University, Raleigh, NC, 27695, USA*

So far, several traditional chromatographic and spectroscopic methodologies have been employed for the qualitative and quantitative analysis of OZP in both clinical and pharmaceutical settings.[11–15] While these techniques are well-known for performing this type of testing, they are associated with several limitations, including reliance on expensive instrumentation, the utilization of labor-intensive workflows, the need for highly trained personnel, and the requirement of extensive sample preparation.

In contrast, electrochemical techniques with a low detection limit, high specificity, and desirable sensitivity have emerged as versatile analytical platforms across several areas, including forensic science, clinical diagnostics, food safety, environmental monitoring, and pharmaceutical detection.[3,16–18] For instance, Muthusankar *et al.* used a nanocomposite containing sulfur-doped carbon quantum dots and iron(III) oxide nanoparticles for the surface modification of a glassy carbon electrode to develop an electrochemical sensing platform for olanzapine detection.[19] The analytical results demonstrated that this sensing platform provided good electrocatalytic activity towards OZP, with a lower detection limit of approximately 0.006 μM. Mahmoud *et al.* used nanocellulose and nitrogen, sulfur co-doped graphene quantum dots for the surface modification of a glassy carbon electrode; this electrode was used for electrochemical detection of OZP, and demonstrated a detection limit of 0.5×10^{-8} M.[20] More recently, Yazan *et al.* decorated a pre-anodized pencil graphite electrode using gold nanoparticles and poly(L-alanine) for the electrochemical detection of OZP; this approach provided a lower detection limit of 0.081 μM.[21] Although these efforts are associated with advantages in terms of sensitivity and analytical performance, certain electrode materials (*e.g.*, glassy carbon electrodes or pencil graphite electrodes) are not well-suited for on-site or real-time monitoring applications. Additionally, these sensing platforms involve the use of multiple reagents, complex surface modification protocols, complicated laboratory instrumentation, prolonged synthesis procedures, and elevated costs; thus, these platforms are not able to measure OZP levels in a point-of-care manner. As such, the development of a miniaturized, scalable, and minimally invasive sensing approach that can overcome the previously mentioned limitations through real-time, on-site detection of OZP concentrations in interstitial fluid with improved analytical sensitivity, selectivity, and reliability is highly desirable.

In recent years, the emergence of wearable and portable sensing technologies, including wrist-worn devices, skin patches, microneedle arrays, smart textiles, contact lenses, minimally invasive implantable sensors, and oral sensors has drawn substantial attention from the scientific community, driven by their potential use in user-friendly, customizable, and point-of-care healthcare devices.[22–35] Among the various wearable sensing strategies that have been evaluated, microneedle-based platforms have garnered significant interest due to their capability for rapid, minimally invasive, and straightforward monitoring of a broad spectrum of biomarkers within interstitial fluid.[36–41] Owing to their micrometer-scale dimensions and minimally invasive design, microneedles are capable of penetrating the stratum corneum, the outermost layer of human skin, to form transient microchannels, facilitating the detection of biologically relevant molecules with minimal discomfort and negligible tissue damage.[42–45] These microneedle-based wearable electrochemical sensors typically incorporate biosensing electrodes at the tips of the microneedle array; these sensors may be used for real-time, multiplexed detection of several analytes that are found in interstitial fluid.[46–48] Because of their several advantages, including minimally invasive tissue-sensor interactions, high sensitivity, and potential use for continuous monitoring, microneedle-based sensing systems have been successfully utilized for the detection of several types of biologically relevant analytes such as ketones, potassium ions, alcohol, dopamine, cholesterol, lidocaine, glucose, L-DOPA, and lactate.[49–55] Despite this progress, to the best of our knowledge, no prior work has described the development of laser-induced graphene on the tips of carbon-coated 3D-printed microneedle arrays for electrochemical sensing of drug molecules in interstitial fluid.

In this work, we have prepared laser-induced graphene on the tips of a carbon-coated 3D-printed microneedle array; this approach was used for the fabrication of a wearable electrochemical sensor to detect OZP in interstitial fluid (Fig. 1). While LIG-based electrochemical sensors and microneedle-based sensing platforms have been explored previously, this study introduces several distinct innovations that advance the state of the art. Notably, we demonstrate one of the earliest integrations of laser-induced graphitization directly with high-resolution 3D-printed microneedles, enabling the formation of high surface-area conductive electrodes without the need for metal deposition, transfer processes, or complex microfabrication. Through an innovative and unique working-electrode microneedle design, selective LIG formation was achieved uniformly along the microneedle sidewalls, which is particularly challenging for curved, high-aspect-ratio structures. This wearable sensing platform integrates microneedle technology, 3D printing, spray coating, and CO_2 infrared laser irradiation approaches to prepare a microneedle-based three-electrode electrochemical system. Carbon and silver conductive inks were deposited onto a custom-designed ultrasharp 3D-printed microneedle array using spray coating in order to form the working, counter, and reference electrodes. To improve the conductivity and enhance the sensitivity, a CO_2 infrared laser was used to modify the surface of a carbon-coated 3D-printed microneedle array-based working electrode into a graphitic structure on the tips of the microneedle array. Prior to OZP detection, the morphological, structural, electrochemical, and analytical properties of the microneedle-based device were characterized. Under the optimized conditions, the microneedle-based sensing platform exhibited high sensitivity and specificity toward OZP. The feasibility for real-time monitoring was validated by examining the analytical characteristics of the sensor towards OZP in artificial interstitial fluid while penetrating a skin-mimicking parafilm model and phantom gel matrix, which indicated the potential and practicability of the sensor for minimally invasive monitoring of antipsychotic drugs. The obtained results emphasize the viability of this cost-effective,

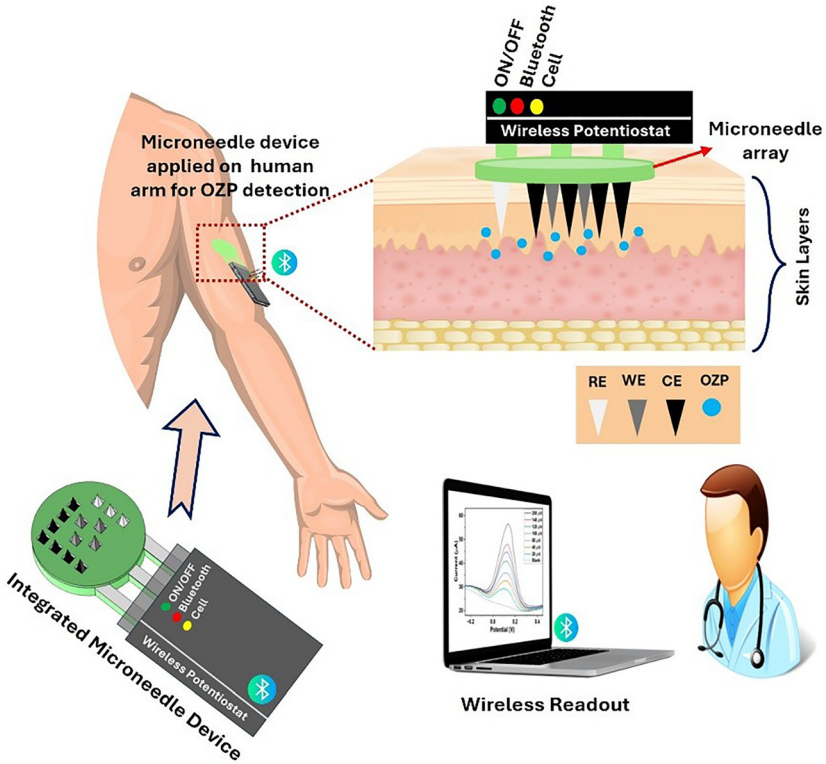

Fig. 1 Schematic illustration of an integrated wearable microneedle sensor applied on the human arm for wireless detection of the drug olanzapine.

scalable, and minimally invasive wearable platform, enabled by 3D printing, for wireless detection of OZP; this processing approach is adaptable to the development of many other types of wearable biosensors.

2. Experimental section

2.1 Materials and methods

The commercial-grade conductive ink (carbon black JR-700 LV, exhibiting a resistivity of 0.7 to 0.9 Ohm-cm), paper, glass, plastics, and metal substrates and silver paste were obtained from NovaCentrix (Round Rock, Texas, USA). All of the chemicals (*e.g.*, potassium ferricyanide and phosphate buffer), target analytes (*e.g.*, OZP), and interfering compounds (*e.g.*, ascorbic acid, citric acid, acetaminophen, uric acid, caffeine, and dopamine) were sourced from Sigma Aldrich (St. Louis, Missouri, USA). Fresh deionized water (18.2 MΩ cm at 25 °C) was obtained from a Milli-Q system (St. Louis, Missouri, USA) for all solution and dilution preparations. All of the other analytical grade reagents were used as received without further modification.

2.2 Design and fabrication of microneedles

An ultra-sharp microneedle array consisting of 14 pyramid-shaped needles (7 for the counter electrode, 4 for the working electrode, and 3 for the reference electrode) was designed using SolidWorks 2016 (Dassault Systèmes, Vélizy-Villacoublay, Yvelines, France). Each needle featured a square base of 600 μm per side and a height of 1800 μm. The array was fabricated using a Boston micro fabrication (BMF) S130 3D printer (Maynard, Massachusetts, USA), which utilizes projection micro stereolithography (PμSL) technology. For the high-resolution 3D printing process, the SolidWorks file was converted into a printer-compatible format by slicing it into digital layers using BMF Slicer software. This process generated a machine-readable code that was compatible with the BMF S130 3D printer. A yellow-colored photoreactive BIO resin (BMF, Maynard, Massachusetts, USA) was used as the printing material; this material was previously validated for biocompatibility by the manufacturer through standardized tests, including the ISO 10993-12:2012 (acute systemic toxicity) test, the ISO 10993-12:2012 (*in vitro* cytotoxicity) test, and the ISO 10993-10:2010, ISO 10993-12:2012, and ISO 10993-2:2006 (skin irritation) tests. The mechanical properties of the cured BIO resin were previously evaluated using a Ubi-1 nanoindenter (Hysitron, Eden Prairie, Minnesota, USA) equipped with a Berkovich diamond tip; the measured Young's modulus was 3.29 ± 0.12 GPa, and the measured hardness was 302.19 ± 10.44 MPa (reported as mean ± standard deviation).[44] Following the 3D printing process, the fabricated microneedle arrays were rinsed in isopropyl alcohol to remove residual unpolymerized resin. Post-curing was performed by exposing the structures to a 405 nm wavelength light source (Formlabs Inc., Somerville, Massachusetts, USA) at 45 °C for 10 minutes to ensure complete polymerization. To modify the 3D-printed microneedle array

into a three-electrode system, commercially-obtained carbon and silver conductive inks were deposited using an air spray coating technique. To ensure the selective deposition, only the regions designated for electrode formation were exposed to the spray; the rest of the part was carefully masked using adhesive tape. The microneedle array was securely mounted onto a custom platform to ensure uniform coating, and a fine airbrush system was used to spray each ink selectively according to a predefined electrode pattern. Spray parameters such as nozzle-to-substrate distance, air pressure, and spray duration were optimized to achieve uniform coverage, while preserving the microneedle geometry. Following ink deposition, the coated array was cured in a conventional oven at 100 °C for 15 minutes to enhance adhesion and conductivity. To establish reliable electrical connections, conductive silver epoxy was applied along the electrode contact leads and allowed to cure at 80 °C for 25 minutes.

2.3 Laser-induced graphene on microneedles

A CO_2 laser machine (Universal Laser Systems, Inc., Scottsdale, Arizona, USA) operating at a wavelength of 10.06 μm was used to modify the surface of a carbon-coated 3D-printed microneedle array-based working electrode into a graphitic structure on the tips of the microneedle array (Fig. S1a). To determine optimal laser parameters for effective carbon-to-graphene conversion, preliminary tests were conducted using a flat 3D-printed substrate that was uniformly coated with the same carbon ink, while maintaining consistent coating parameters.[56] The laser beam was intentionally defocused by 2 mm above the substrate to produce a broader, thermally diffused spot and less aggressive irradiation profile, minimizing potential damage to the underlying polymer structure (Fig. S1b). A series of laser power settings ranging from 12% to 17% (in 1% increments) was applied, while keeping the scanning speed and *Z*-axis height constant. This controlled defocused irradiation allowed for localized thermal treatment, promoting graphitization without damaging the 3D-printed parts. Once the laser power was optimized, the carbon-coated 3D-printed microneedle array was affixed onto a custom 3D-printed block angled at 60° using double-sided adhesive tape to ensure stable positioning and exposure (Fig. S1c). The mounted array was then placed inside the laser system at the same 2 mm defocused height and irradiated at the optimized power settings. To ensure uniform graphitization across all four lateral surfaces of the microneedles, the array was rotated 90° clockwise for each of four successive laser exposures. The laser-treated microneedle array was subsequently characterized using scanning electron microscopy (SEM) to assess morphological changes and confirm localized surface modification. Raman spectroscopy was employed to verify the structural transformation of the carbon layer, particularly *via* assessment of the characteristic D and G bands that are indicative of graphitic carbon. After these analyses and confirmation of the successful formation of graphitic domains on the microneedle tips and bases, the laser-treated microneedle array was used as a working electrode in the three-electrode electrochemical sensing system.

2.4 Physical and electrochemical characterization

The topological and morphological characteristics of the 3D-printed microneedle arrays, both before and after laser treatment of the carbon-coated microneedles, were evaluated using a SU3900 variable pressure scanning electron microscope (VP-SEM) (Hitachi, Tokyo, Japan); this instrument is equipped with a solid-state backscattered electron (BSE) detector and is capable of operating across an accelerating voltage range of 0.3 kV to 30 kV. Raman spectroscopy was employed to assess the structural transformation of the carbon coating into graphitic domains following laser treatment. The electrochemical characterization of the three-electrode electrochemical sensing system on the microneedle arrays was carried out using a battery-powered, handheld PalmSens4 potentiostat (PalmSens BV, Houten, Netherlands). This portable device enabled comprehensive wireless electrochemical testing at room temperature, such as cyclic voltammetry (CV) and differential pulse voltammetry (DPV), for assessing electrode stability, analyte detection sensitivity, temporal signal stability, and interference response. Data acquisition and transfer were performed wirelessly *via* Bluetooth, facilitating real-time monitoring and subsequent data analysis without the need for tethered instrumentation.

2.5 Electrochemical sensing of OZP

Prior to evaluating the OZP sensing capability of the microneedle-based electrochemical platform, the electrochemical characteristics and stability of the carbon-coated conductive microneedle working electrode were evaluated using cyclic voltammetry (CV) in a 3 mM potassium ferricyanide solution prepared in 0.1 M phosphate buffer (pH 7.4) at a fixed scan rate of 50 mV s^{-1}; studies were performed to assess redox activity, electron transfer efficiency, and current response stability over repeated cycles. Subsequently, the electrochemical performance of the three-electrode system was re-assessed after laser treatment of the carbon-coated microneedle working electrode, which generated graphitic structures and improved electrical conductivity at the microneedle tips. CV measurements under the same experimental conditions were obtained to assess enhancements in peak current response, electrochemical reversibility, and overall electron transfer efficiency resulting from the laser-induced surface modification. For quantitative analysis of OZP, various concentrations of OZP were freshly prepared by diluting the 1.0 mg mL^{-1} stock solution into fresh supporting phosphate buffer electrolyte; DPV measurements were collected for each concentration over a potential window from −0.2 V to +0.5 V *vs.* Ag/AgCl using a pulse time of 20 ms and a potential step of 10 mV. The corresponding DPV spectra were used to determine sensitivity, linear dynamic range, and limit of detection. For each experiment, including the calibration curves, we tested $n = 3$ independently fabricated sensors. Furthermore, to evaluate the long-term storage stability of the sensor, the electrochemical response toward a fixed concentration of OZP was measured periodically over a span of three weeks under ambient storage conditions. Variations in peak current intensity, potential shifts, and signal reproducibility

were analyzed to quantify degradation effects and validate the operational reliability of the microneedle-based sensing platform.

2.6 Proof-of-concept study

To evaluate the practical applicability and real-time sensing performance of the fully assembled microneedle-based electrochemical sensor, the electrochemical response of the laser-treated carbon-coated microneedle working electrode was evaluated using artificial interstitial fluid (ISF) using both a skin-mimicking parafilm interface and a phantom gel model *via* DPV.[44] In the first model, a Petri dish containing artificial ISF was spiked with varying concentrations of OZP, followed by sealing the solution surface with a stretched parafilm layer to mimic the mechanical resistance of the skin. The microneedle-based sensor assembly was then gently pressed against the parafilm, ensuring that the microneedle tips penetrated the membrane and reached the underlying fluid layer to facilitate analyte–electrode interaction. The DPV measurements were recorded over a potential window of −0.25 V to +0.5 V *vs.* Ag/AgCl, with a potential step of 10 mV. In the second model, a skin-analogous phantom gel matrix was fabricated according to previously established protocols to simulate the viscoelastic and ionic properties of human dermal tissue. The OZP-spiked phantom gel was brought into contact with the microneedle sensor; after a fixed diffusion period of 3 minutes, the DPV signal was recorded under identical electrochemical parameters. This approach enabled evaluation of the microneedle penetration and detection capabilities of the sensing platform in a more physiologically relevant medium to understand its feasibility for use in transdermal sensing applications.

3. Results and discussion

3.1 Design and working of the microneedle sensor

The development of conductive microneedle array-based platforms for minimally invasive sensing of pharmacological and physiological biomarkers is emerging as a transformative technology for wearable diagnostics. While earlier approaches have primarily relied on metallic microneedles to construct electrochemical working electrodes, their high fabrication costs, material rigidity, and limited scalability have hindered widespread adoption of microneedle technology.[57,58] To overcome these challenges, we developed a cost-effective, scalable, and customizable microneedle-based electrochemical sensing system by leveraging additive manufacturing techniques, including high-resolution 3D printing, selective air-spray deposition, and laser-induced graphitization. A schematic overview of the fabrication workflow of the fully integrated microneedle device is presented in Fig. 2. The desired microneedle array geometry was first designed using SolidWorks and fabricated *via* a projection micro-stereolithography (PμSL)-based BMF S130 3D printer with a biocompatible photopolymer resin. Following 3D printing, the array was selectively masked and coated with carbon and silver inks *via* air-spray deposition to establish conductive paths for the working, counter, and reference electrodes. The central portion of the array, designated as the working electrode, was coated with carbon ink and subsequently subjected to CO_2 laser-induced graphitization to enhance surface conductivity and electrocatalytic activity by locally converting the amorphous carbon into graphitic domains at the microneedle tips as well as on the base. The left L-shaped region coated with carbon ink functioned as the counter electrode. The right strip was coated with Ag/AgCl paste; it was assigned as the reference electrode. Next, electrical interconnects were established by applying a conductive silver epoxy along the connecting legs, followed by thermal curing. To ensure operational stability and prevent electrical shorting, a thin, custom 3D-printed insulating cover was aligned and attached over the microneedle base, exposing only the tips for analyte interaction. Furthermore, for a proof-of-concept demonstration, the fully integrated microneedle device was then interfaced with a portable, battery-powered wireless PalmSens4 potentiostat and utilized for the electrochemical detection of OZP. The recorded electrochemical signals were wirelessly transmitted to a local computing device for real-time data acquisition and analysis, demonstrating the feasibility of this sensing device for decentralized and continuous transdermal biosensing.

3.2 Fabrication, graphitization, and evaluation of the conductive microneedle array

Advancements in computer-aided design software and high-resolution 3D printers have significantly streamlined the fabrication and customization of microneedle arrays, allowing

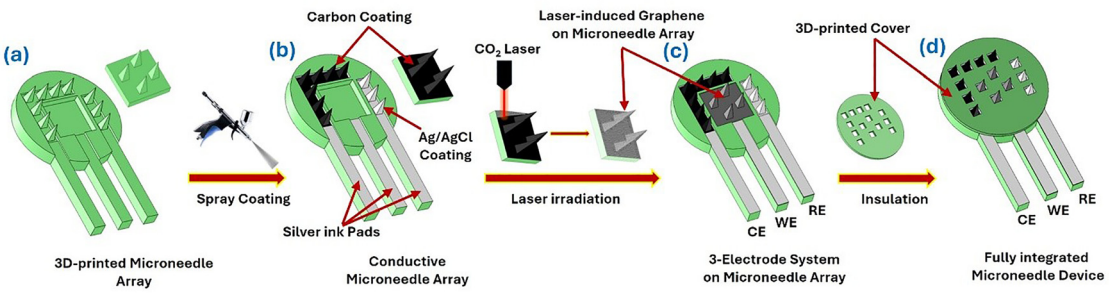

Fig. 2 Schematic illustration of the step-by-step fabrication procedure for the development of laser induced graphene on the tips of the carbon-coated microneedle array: (a) 3D-printed microneedle array, (b) air-spray deposition of carbon and silver inks on the 3D-printed microneedle array, (c) laser-induced graphitization of the carbon-coated working electrode 2 × 2 microneedle array, and (d) fully integrated microneedle device.

precise control over their geometry, dimensions, and spatial configuration. These scalable manufacturing techniques have emerged for the cost-effective and rapid fabrication of complex biomedical and wearable healthcare devices. In this study, we leveraged these capabilities to develop a highly specialized microneedle array tailored for transdermal biosensing applications. A microneedle array comprising 14 pyramid-shaped needles was designed using SolidWorks 2016 software. Each microneedle was engineered with a height of 1800 μm and a square base measuring 600 μm per side to ensure sufficient mechanical strength and skin penetration efficiency while minimizing tissue damage. The designed array was subsequently fabricated using a BMF S130 3D printer, which employs PμSL technology for high-fidelity printing of microscale features. Given the requirement for controlled skin insertion and minimal invasiveness, a photoreactive, biocompatible BIO resin (yellow color) supplied by BMF was selected as the printing material. This resin exhibits mechanical properties, including Young's modulus and hardness, which are sufficient for transdermal penetration through the stratum corneum layer of the epidermis.[38]

A detailed stepwise visual representation containing photos of each stage of the fabrication process is provided in Fig. 3, demonstrating the integrated design and manufacturing strategy employed in developing the microneedle-based sensing platform. The initial 3D-printed microneedle array, as depicted in Fig. 3a, served as the base structure for subsequent functionalization. The selective deposition of conductive inks was achieved using an air spray coating technique, enabling patterning of conductive materials onto predefined regions of the array. A macroscopic image of the spray-coated microneedle array following this deposition process is presented in Fig. 3a. To configure the electrochemical sensing interface, a three-electrode configuration was established directly on the microneedle array surface. The central 2 × 2 region, previously coated with carbon ink, was designated as the working electrode and further modified by locally converting the amorphous carbon into graphitic domains at the microneedle tips (Fig. 3b) as well as on the base *via* laser treatment to enhance surface conductivity and facilitate electron transfer kinetics.[59] In addition to the optical image, a short video (SI, Video S1) of the laser-induced graphitization of the carbon-coated 3D-printed microneedle array using a CO_2 laser was also recorded and incorporated in the SI. Following the graphitization of the working electrode, a thin biopolymeric protective layer was applied to the working electrode to prevent potential leaching and ensure mechanical stability during transdermal insertion. The right-side 1 × 3 array was functionalized with Ag/AgCl paste to serve as the integrated reference electrode; the L-shaped region coated with carbon ink was assigned as the counter electrode. A final encapsulation step was performed to electrically isolate the conductive traces and contact pads, leaving only the microneedle tips exposed for analyte interaction. The fully assembled sensing unit, housed within a 3D-printed protective cover, is shown in Fig. 3c; this figure shows the completed microneedle-based platform prepared for subsequent electrochemical characterization and biosensing studies. To characterize the microscale morphology of the fabricated microneedle structures, scanning electron microscopy (SEM) was employed to capture the three-dimensional topographical features of the laser-treated and untreated carbon-coated microneedles. Representative SEM micrographs of the pristine carbon-coated microneedle and laser-induced graphitic domains on the carbon-coated microneedle are presented in Fig. 4. Fig. 4a and b present SEM micrographs of the tips of an individual pristine carbon-coated microneedle and laser-treated carbon-coated microneedles, respectively. These images demonstrate the sharpness of the microneedle tips, with well-defined apex geometries and diameters of approximately 5–6 μm, even after the carbon coating and laser treatment of microneedles; this feature is critical for efficient skin penetration while minimizing tissue damage. Fig. 4c and e show the magnified SEM images of pristine carbon-coated microneedles at different magnifications. These images demonstrate the consistent and uniform coating of the carbon ink along the microneedle surface, with no evidence of large aggregates or coating irregularities, which can be noticed in depositions made *via* the air spray coating technique. Next, Fig. 4d and f show the magnified SEM images of laser-treated carbon-coated microneedles at different magnifications, demonstrating the significantly

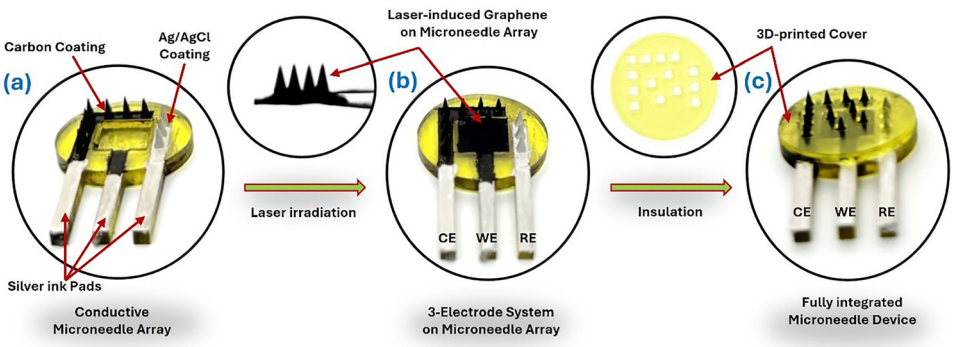

Fig. 3 Real images of (a) silver ink-coated contact pads and carbon-coated 3D-printed microneedle array, (b) laser-induced graphitization of carbon-coated 2 × 2 microneedle array-based working electrode, and (c) fully shielded and integrated 3-electrode arrangement on the tips of the microneedles.

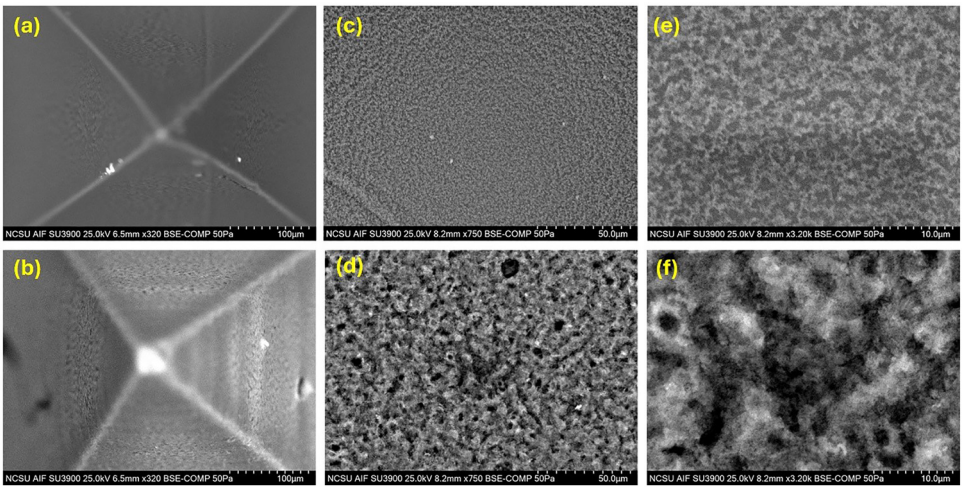

Fig. 4 Demonstration of scanning electron microscope (SEM) images of a pristine carbon-coated microneedle and laser-induced graphitic domains on a carbon-coated microneedle. SEM micrographs of (a) the tip of a single carbon-coated microneedle, (b) the tip of a laser-treated carbon-coated microneedle, (c) and (e) magnified SEM images of carbon-coated microneedles at different magnifications, and (d) and (f) magnified SEM images of laser-treated carbon-coated microneedles at different magnifications.

increased surface roughness and microscale porosity as compared to the pristine carbon-coated microneedles. These changes in the surface morphology are attributed to localized thermal effects induced by the laser, confirming the successful conversion of the originally smooth carbon layer into a more electroactive graphitic structure at the tips of the microneedles. Next, the ability to effectively penetrate skin is a critical factor in assessing the practical use of microneedle-based devices for transdermal sensing. Accordingly, the skin penetration performance of the as-printed microneedle array was evaluated using a porcine skin patch (*ex vivo*). The optical image (shown in the SI, Fig. S2) of the skin patch after microneedle insertion and Trypan Blue treatment clearly demonstrates that the microneedle array penetrated the skin in a controlled and topographically confined manner, without causing damage to the surrounding tissue. This result confirms the suitability of the developed microneedle array for transdermal applications.

To understand the structural transformation of the carbon coating that was induced by laser treatment, Raman spectroscopy was performed on both pristine and laser-treated carbon-coated microneedle arrays. Fig. 5a contains the Raman spectra of both the pristine carbon-coated microneedle array, abbreviated as CCMN, and the laser-induced graphene on the tips of the carbon-coated microneedle array, abbreviated as LIGMN. It can be noticed that the intensity of characteristic D ($\sim$1340 cm^{-1}) and G ($\sim$1580 cm^{-1}) bands of CCMN is relatively low, suggesting a predominantly amorphous carbon structure.[60] However, the Raman spectrum of the LIGMN exhibits very strong characteristic D and G bands associated with structural disorder and an increase in sp^2-hybridized carbon domains.[61] Furthermore, a parallel reduction in the 2D band intensity was observed in the laser-treated samples, which can be attributed to several laser-induced effects, including increased structural disorder, generation of additional defects, and changes in local strain within the carbon matrix.[61,62] These spectral changes, along with the SEM images, confirm the successful photothermal conversion of the carbon film into an electrochemically favorable graphitic structure at the microneedle tips.

3.3 Electrochemical response, olanzapine sensing, and selectivity assessment

Before employing the developed microneedle-based sensor for the electrochemical quantification of OZP, a systematic investigation of redox characteristics and operational stability of the integrated three-electrode configuration on the tips of the microneedle array was conducted. Cyclic voltammetry measurements were performed in a freshly prepared 3 mM potassium ferricyanide solution (in 0.1 M phosphate buffer, pH 7.4) at a fixed scan rate of 50 mV s^{-1} in order to characterize the charge transfer efficiency of the microneedle electrodes. As shown in Fig. 5b, the cyclic voltammetry response of the pristine carbon-coated microneedle working electrode (green trace) exhibits a quasi-reversible redox profile, with well-defined anodic and cathodic peaks, confirming effective electron transfer at the electrode/electrolyte interface. To assess the influence of laser-induced surface modification, a comparative cyclic voltammetry measurement was conducted using the laser-treated carbon-coated microneedle array (red trace, Fig. 5b) as the working electrode; a significant improvement in peak current was observed following laser treatment, suggesting enhanced electrochemical kinetics. This enhancement in the electron transfer activity is attributed to increased surface roughness, a higher density of electroactive defect sites, and the occurrence of graphitic domains introduced by localized CO_2 laser irradiation, as confirmed by SEM and Raman spectra analysis. These surface changes collectively improve electron transfer rates and interfacial accessibility, thereby enhancing the electroanalytical characteristics of the microneedle-based working electrode. Since the operational reliability of microneedle-based

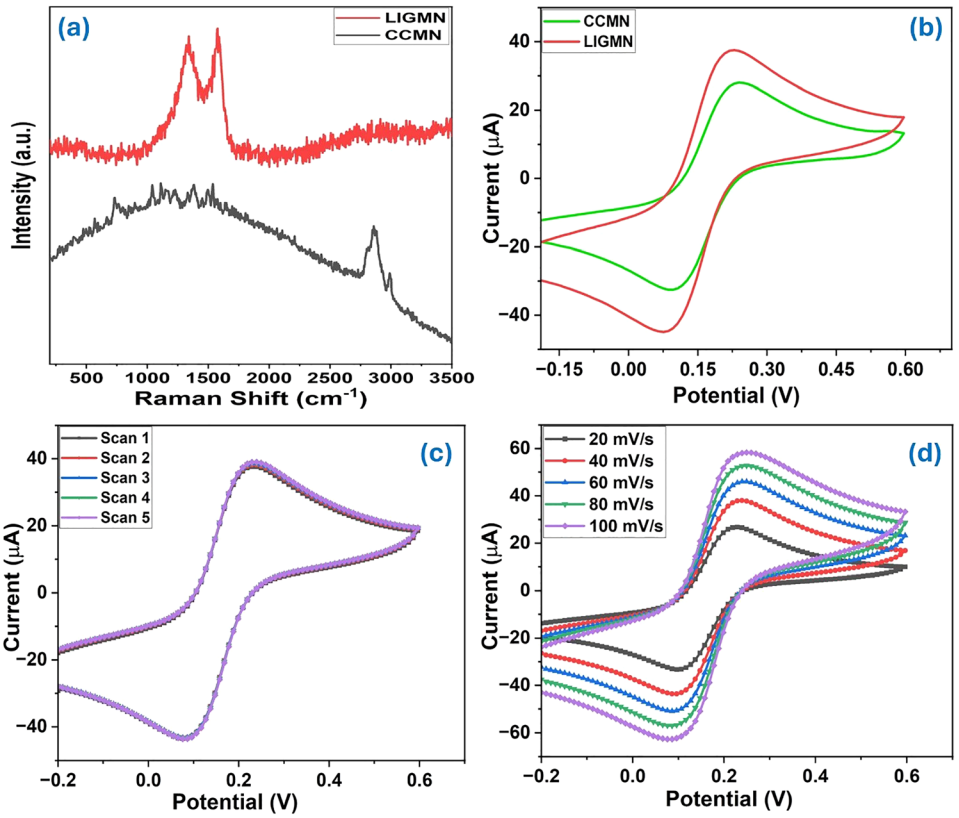

Fig. 5 Demonstration of the Raman spectra, redox response, and stability of the fabricated microneedle-based sensor. (a) Raman spectra of the pristine carbon-coated microneedle array (CCMN, black track) and laser induced graphene on the tips of the carbon-coated microneedle array (LIGMN, red track). (b) Cyclic voltammetry spectra of the CCMN (green track) and LIGMN (red track) working electrode. (c) Multiple scans of the laser-treated carbon-coated microneedle array in 3 mM ferricyanide solution at 50 mV s^{-1} and (d) cyclic voltammograms recorded at varying scan rates ranging from 20 mV s^{-1} to 100 mV s^{-1} using the laser-treated carbon-coated microneedle array.

electrochemical sensors is dependent on the consistency of their redox behavior, the electrochemical stability of the laser-treated carbon-coated microneedle working electrode was further assessed. This evaluation was performed by recording five successive cyclic voltammetry scans under identical experimental conditions in a 3 mM ferricyanide solution. As shown in Fig. 5c, the cyclic voltammograms exhibited excellent reproducibility, with highly overlapping oxidation and reduction peaks across all scans. This high degree of overlap indicates minimal variation in electron transfer dynamics, confirming the robust electrochemical stability and repeatability of the three-electrode microneedle platform; this feature is an essential requirement for reliable detection of olanzapine in real biological environments. To further elucidate the interfacial charge transfer characteristics and redox kinetics of the laser-treated carbon-coated microneedle working electrode, a scan rate-dependent cyclic voltammetry study was performed. The cyclic voltammograms recorded at varying scan rates over a range from 20 mV s^{-1} to 100 mV s^{-1} are shown in Fig. 5d. Fig. 5d shows that with increasing scan rate, the anodic peak potential shifts progressively toward more positive values, while the cathodic peak potential shifts toward more negative values, revealing the quasi-reversible redox process governed by surface-confined electron transfer kinetics.

3.4 Olanzapine sensing and selectivity assessment

After examining the electrochemical characteristics, redox behavior, and electrode stability of the microneedle-based three-electrode system, the analytical functionality of the laser-treated carbon-coated microneedle working electrode toward various concentrations of OZP was evaluated using differential pulse voltammetry. The widely accepted therapeutic plasma concentration of OZP is 20–80 ng mL^{-1} (64 nM to 256 nM) as recommended by therapeutic drug monitoring (TDM) guidelines.[63,64] Concentrations above 80 ng mL^{-1} are associated with an increased risk of adverse effects, while levels $\geq$ 100 ng mL^{-1} are generally considered to fall within a toxic or alert range. Since ISF-based sensing research is still in its early stages, no standardized therapeutic range for OZP in interstitial fluid (ISF) has been established to this point, as routine clinical monitoring continues to rely on plasma measurements. However, because ISF (produced through capillary filtration of blood) closely resembles plasma in composition and is considered the most compelling alternative to blood for minimally invasive monitoring,[65] we designed and tested our microneedle-based sensor, ranging from 50 nM to 500 μM, to overlap with the clinically relevant OZP concentration range observed in plasma. As shown in Fig. 6a, the differential pulse voltammetry spectra reveal a concentration-dependent increase

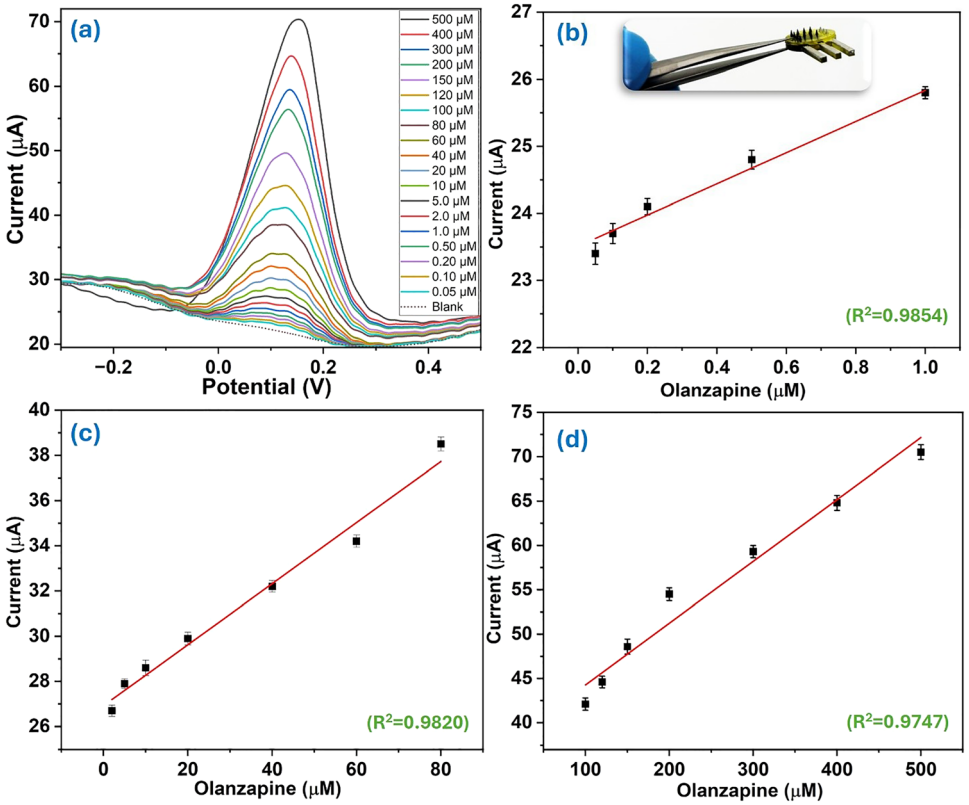

Fig. 6 Demonstration of the electrochemical sensing potential of the fabricated microneedle-based sensing platform. (a) Differential pulse voltammogram of the laser-treated carbon-coated microneedle-based working electrode corresponding to an increasing OZP concentration ranging from 0.05 to 500 μM. An illustration of the calibration curve between the peak current values and OZP concentration for (b) low (0.05–1.0 μM), (c) intermediate (2.0–80 μM), and (d) high concentration ranges (100–500 μM). Inset: Real photo of the developed microneedle-based sensors used for sensing experiments.

in the oxidation peak current with increasing OZP concentration ranging from 0.05 to 500 μM; this result indicates efficient electrochemical oxidation of OZP at the modified microneedle surface. For quantitative analysis of the sensing probe, the peak current values were plotted against the corresponding OZP concentrations across a broad dynamic range (0.05 to 500 μM). For enhanced analytical resolution, the calibration data were segmented into three linear regions, specifically low (0.05–1.0 μM), intermediate (2.0–80 μM), and high concentration ranges (100–500 μM). It was noted that each range exhibited strong linearity between the current response and OZP concentration, with correlation coefficients (R^2) of 0.985, 0.982, and 0.9747, respectively (Fig. 6b–d). Furthermore, the limit of detection for OZP was calculated using the standard equation ($3s/M$, where s represents the standard deviation of the blank signal and M is the slope of the calibration curve), and was determined to be as low as 0.0026 μM, highlighting the high sensitivity of the microneedle-based sensing platform. These results confirm the desirable sensitivity and wide dynamic detection capability of the microneedle sensor, making it suitable for both trace-level monitoring and therapeutic concentration monitoring of OZP in bioanalytical and pharmaceutical applications. While the obtained electroanalytical results confirm the sensing capability of the microneedle-based sensing platform, understanding the selectivity of the sensor toward OZP in the presence of possible interfering substances is critical for appropriate performance in complex biological environments. To assess the selectivity of the microneedle-based electrochemical sensor toward OZP, interference studies were conducted using common electroactive biomolecules, including ascorbic acid, caffeine, uric acid, acetaminophen, and dopamine. Differential pulse voltammetry responses were recorded after sequentially introducing each interferent at a fixed concentration of 50 μM, while maintaining all other experimental parameters constant. As shown in Fig. 7a, minor variations in peak current were observed for the interfering species; however, the response corresponding to OZP remained distinct and well-defined. Furthermore, the anti-interference performance of the sensor to selectively detect the target analyte in the presence of potential interferents was assessed through chronoamperometry, and an immediate change in the current value upon successive addition of OZP even in the presence of interferents was observed (shown in the SI Fig. S3), confirming the strong anti-interference performance of the sensor. These results confirm that the sensor exhibits adequate selectivity toward OZP, even in the presence of structurally or electrochemically similar compounds; moreover, these results support the applicability of the microneedle-based sensing platform for real-time monitoring in physiologically relevant environments.

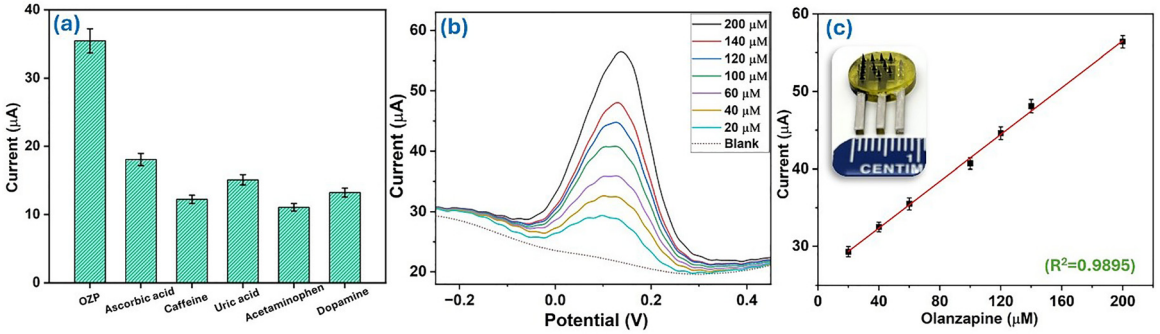

Fig. 7 Illustration of the selectivity assay and the proof-of-concept study of the fully assembled microneedle-based sensing system. (a) Demonstration of peak current values recorded during selectivity studies after sequentially introducing each interferent at a fixed concentration of 50 μM, (b) differential pulse voltammetry spectra recorded during OZP detection in artificial interstitial fluid through a skin-mimicking parafilm layer, and (c) respective calibration curve for various OZP concentrations spiked in artificial interstitial fluid and the obtained peak current values (inset: macroscopic image of the microneedle array-based sensors used in the proof-of-concept study).

3.5 Proof-of-concept demonstration in skin-mimicking models and long-term stability

After the electrochemical sensing performance of the laser-treated carbon-coated microneedle-based platform was demonstrated, its applicability for the detection of OZP in practical settings was systematically investigated using a skin-mimicking parafilm model and a phantom gel matrix. A Petri dish was covered with parafilm, which served as a synthetic skin barrier, and was filled with artificial interstitial fluid; the fluid was spiked with increasing concentrations of OZP. Next, the differential pulse voltammetry measurements were collected within a potential range of −0.25 V to 0.5 V, with a step potential of 0.01 V. The recorded voltammetry measurements (shown in Fig. 7b) demonstrated a smooth increase in oxidation peak current, corresponding to each added OZP concentration (20 μM to 200 μM), indicating appropriate transdermal sensing functionality of the microneedle-based sensor. A calibration curve, which was created by plotting peak current *versus* OZP concentration (Fig. 7c), displayed a good linear relationship with correlation coefficients (R^2) of 0.9895; this result indicated the high sensitivity and quantitative detection potential of the microneedle-based sensor. To further validate the practical applicability of the microneedle sensor, OZP detection was also performed in a tissue-mimicking phantom gel matrix spiked with different OZP concentrations ranging from 20 μM to 150 μM. As shown in Fig. 8a, the sensor exhibited distinct current responses across all of the OZP concentrations that were tested in the phantom gel. Furthermore, the corresponding calibration plot (Fig. 8b) between the peak current values and varying OZP concentrations maintained excellent linearity with correlation coefficients (R^2) of 0.9890. These proof-of-concept studies collectively confirm the robust performance of the microneedle-based electrochemical sensor for reliable, minimally invasive detection of OZP in physiologically appropriate conditions. The long-term operational stability of the fully integrated microneedle-based electrochemical sensor was assessed by monitoring its sensing performance at five-day intervals over a 20-day storage period at room temperature with dry conditions in a closed, dust-free container (without exposure to humidity or light). As illustrated in the bar graph (Fig. 8c), the sensor retained approximately 87% of its original electrochemical response after 20 days, indicating minimal degradation in analytical performance. These findings indicate the structural integrity and functional durability of the laser-treated carbon-coated microneedle array, highlighting its potential use for the transdermal detection of micromolar concentrations of OZP.

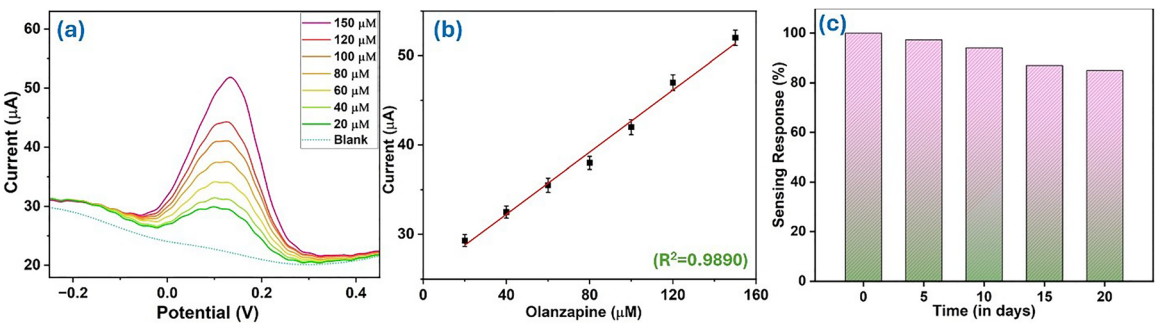

Fig. 8 Demonstration of practical applicability and long-term operational stability of the fully assembled microneedle sensor. (a) Differential pulse voltammogram recorded during OZP detection in a tissue-mimicking phantom gel matrix spiked with different OZP concentrations ranging from 20 μM to 150 μM, (b) respective calibration curve of various OZP concentrations and the obtained peak current values, and (c) demonstration of the long-term operational stability of the fabricated microneedle sensor at 5-day intervals over a 20-day storage period under ambient conditions.

4. Conclusions

In this work, we developed a scalable and cost-effective electrochemical point-of-care platform using a laser-treated carbon-coated microneedle array for the minimally invasive detection of OZP. The microneedle sensor demonstrated excellent sensitivity, low limit of detection, high selectivity for OZP, and strong linearity in artificial interstitial fluid. The analytical performance demonstrated in physiologically relevant models, including a skin-mimicking parafilm layer and a phantom gel matrix, indicated the practical applicability of the laser-treated microneedle-based platform for transdermal monitoring of antipsychotic drugs. This innovative microneedle sensor platform was created using 3D printing, spray coating, and CO_2 infrared laser irradiation for straightforward assembly, economical manufacturing, and scalable manufacturing. The favorable analytical performance and straightforward fabrication process make the microneedle-based platform appropriate for the development of affordable, wearable, and single-use biosensors to detect biologically relevant molecules in interstitial fluid. In the future, we aim to integrate a multiplexed sensing system and develop a fully wearable patch with a built-in battery and wireless electronics for real-time health monitoring.

Author contributions

Sachin Kadian: conceptualization, methodology, formal analysis, data curation, investigation, writing – original draft preparation, validation, and writing – reviewing and editing. Siba Sahoo: visualization, formal analysis, investigation, and writing – reviewing and editing. Fahad Munshe: formal analysis, investigation, software, and validation. Shubhangi Shukla: writing – reviewing and editing, software and validation. Roger Narayan: visualization, supervision, funding acquisition, resources, project administration, and writing – reviewing and editing.

Conflicts of interest

There are no conflicts to declare for this work.

Data availability

The data collected throughout the course of the study are presented and detailed within the main sections of the manuscript.

Supplementary information (SI) is available. See DOI: https://doi.org/10.1039/d5tb02162f.

Acknowledgements

We acknowledge financial support from the National Science Foundation Award Number 2029974. This work was performed in part at the Analytical Instrumentation Facility (AIF) at North Carolina State University, which is supported by the State of North Carolina and the National Science Foundation (award number ECCS-2025064). The AIF is a member of the North Carolina Research Triangle Nanotechnology Network (RTNN), a site in the National Nanotechnology Coordinated Infrastructure (NNCI).

References

1 D. I. Velligan and S. Rao, The epidemiology and global burden of schizophrenia, *J. Clin. Psychiatry*, 2023, **84**(1), 45094, DOI: 10.4088/JCP.MS21078COM5.
2 C. U. Correll and N. R. Schooler, Negative symptoms in schizophrenia: a review and clinical guide for recognition, assessment, and treatment, *Neuropsychiatr. Dis. Treat.*, 2020, 519–534, DOI: 10.2147/NDT.S225643.
3 J. Thangphatthanarungruang, P. Pasakon, A. Wisitsoraat, A. Tuantranont, V. Intasanta and C. Karuwan, Facile surface modification of the poly (L-cysteine) on 2D-printed reduced graphene oxide electrode to fabricate a highly sensitive electrochemical sensor for determining the antipsychotic drug olanzapine, *Surf. Interfaces*, 2024, **46**, 104145, DOI: 10.1016/j.surfin.2024.104145.
4 S. Shukla, J. Jakowski, S. Kadian and R. J. Narayan, Computational approaches to delivery of anticancer drugs with multidimensional nanomaterials, *Comput. Struct. Biotechnol. J.*, 2023, **21**, 4149–4158.
5 S. Shukla, N. N. Joshi, S. Kadian and R. J. Narayan, Development of drug-loaded PCL@ MOF film enclosed in a photo polymeric container for sustained release, *ACS Appl. Bio Mater.*, 2024, **7**(8), 5382–5396.
6 J. T. Callaghan, R. F. Bergstrom, L. R. Ptak and C. M. Beasley, Olanzapine: pharmacokinetic and pharmacodynamic profile, *Clin. Pharmacokinet.*, 1999, **37**(3), 177–193, DOI: 10.2165/00003088-199937030-00001.
7 K. E. Evoy, S. Humpert, S. Torrez, H. Hussein and J. R. Covvey, Quetiapine and olanzapine misuse prevalence in a US general population sample, *Mental Health Clinician*, 2023, **13**(2), 25–35, DOI: 10.9740/mhc.2023.04.025.
8 P. Łukasiewicz and A. Ferenc, Olanzapina--nadużywanie i nieprawidłowe używanie, *Psychiatr. Psychol. Klin.*, 2022, **22**(1), 67–72, DOI: 10.15557/PiPK.2022.0009.
9 L. Orsolini, C. Tomasetti, A. Valchera, R. Vecchiotti, I. Matarazzo, F. Vellante, F. Iasevoli, E. F. Buonaguro, M. Fornaro, A. L. C. Fiengo, G. Martinotti, M. Mazza, G. Perna, A. Carano, A. De Bartolomeis, M. Di Giannantonio and D. De Berardis, 2016, preprint, DOI: 10.1080/14740338.2016.1201475.
10 L. K. Townsend, W. T. Peppler, N. D. Bush and D. C. Wright, Obesity exacerbates the acute metabolic side effects of olanzapine, *Psychoneuroendocrinology*, 2018, **88**, 121–128, DOI: 10.1016/j.psyneuen.2017.12.004.
11 D. Kang, J. Lu, W. Liu, P. Shao and R. Wu, Association between olanzapine concentration and metabolic dysfunction in drug-naive and chronic patients: similarities and differences, *Schizophrenia*, 2022, **8**(1), 9, DOI: 10.1038/s41537-022-00211-5.
12 J. T. Catlow, R. D. Barton, M. Clements, T. A. Gillespie, M. Goodwin and S. P. Swanson, Analysis of olanzapine in

human plasma utilizing reversed-phase high-performance liquid chromatography with electrochemical detection, *J. Chromatogr. B: Biomed. Sci. Appl.*, 1995, **668**(1), 85–90, DOI: 10.1016/0378-4347(95)00061-M.

13 D. W. Boulton, J. S. Markowitz and C. L. DeVane, A high-performance liquid chromatography assay with ultraviolet detection for olanzapine in human plasma and urine, *J. Chromatogr. B: Biomed. Sci. Appl.*, 2001, **759**(2), 319–323, DOI: 10.1016/S0378-4347(01)00240-7.

14 R. Ahmed, K. P. Bhusari, M. R. Tajne and S. A. Khan, Development of a stability indicating HPTLC method for the estimation of olanzapine in pharmaceutical dosage forms, *J. Indian Chem. Soc.*, 2021, **98**(11), 100215, DOI: 10.1016/j.jics.2021.100215.

15 R. V. Nirogi, V. N. Kandikere, M. Shukla, K. Mudigonda, S. Maurya, R. Boosi and A. Yerramilli, Development and validation of a sensitive liquid chromatography/electrospray tandem mass spectrometry assay for the quantification of olanzapine in human plasma, *J. Pharm. Biomed. Anal.*, 2006, **41**(3), 935–942, DOI: 10.1016/j.jpba.2006.01.040.

16 R. P. Shukla, R. H. Belmaker, Y. Bersudsky and H. Ben-Yoav, A platinum black-modified microelectrode for in situ olanzapine detection in microliter volumes of undiluted serum, *J. Neural Transm.*, 2020, **127**(2), 291–299, DOI: 10.1007/s00702-019-02139-0.

17 H. A. Noureldin, A. Abdelwahab, A. M. Abdel-Aziz, G. M. El-Sayed, A. A. Moustafa and I. H. Badr, Nickel-cobaltite-doped carbon xerogel based voltammetric sensor for olanzapine: Electrochemical characterization and applications, *Microchem. J.*, 2024, **197**, 109758, DOI: 10.1016/j.microc.2023.109758.

18 H. Shahinfard, M. Shabani-Nooshabadi, A. Reisi-Vanani and R. Darabi, Electrochemical sensor based on CuO/reduced graphene nanoribbons and ionic liquid for simultaneous determination of tramadol, olanzapine and acetaminophen, *Carbon Lett.*, 2023, **33**(5), 1433–1444, DOI: 10.1007/s42823-023-00512-4.

19 G. Muthusankar, A. Sangili, S. M. Chen, R. Karkuzhali, M. Sethupathi, G. Gopu, S. Karthick, R. K. Devi and N. Sengottuvelan, In situ assembly of sulfur-doped carbon quantum dots surrounded iron (III) oxide nanocomposite; a novel electrocatalyst for highly sensitive detection of antipsychotic drug olanzapine, *J. Mol. Liq.*, 2018, **268**, 471–480, DOI: 10.1016/j.molliq.2018.07.059.

20 A. M. Mahmoud, M. H. Mahnashi, S. A. Alkahtani and M. M. El-Wekil, Nitrogen and sulfur co-doped graphene quantum dots/nanocellulose nanohybrid for electrochemical sensing of anti-schizophrenic drug olanzapine in pharmaceuticals and human biological fluids, *Int. J. Biol. Macromol.*, 2020, **165**, 2030–2037, DOI: 10.1016/j.ijbiomac.2020.10.084.

21 Ü. N. Tüzün, C. Yıldız, D. Eskiköy Bayraktepe, K. Polat and Z. Yazan, Electrochemical fabrication of poly (L-alanine)-gold nanoparticle nanocomposite-modified electrode: application for determination and mechanism of antipsychotic drug olanzapine, *Monatsh. Chem.*, 2023, **154**(1), 95–104, DOI: 10.1007/s00706-022-03012-9.

22 S. NajafiKhoshnoo, T. Kim, J. A. Tavares-Negrete, X. Pei, P. Das, S. W. Lee, J. Rajendran and R. Esfandyarpour, A 3D nanomaterials-printed wearable, battery-free, biocompatible, flexible, and wireless pH sensor system for real-time health monitoring, *Adv. Mater. Technol.*, 2023, **8**(8), 2201655, DOI: 10.1002/admt.202201655.

23 J. Kim, A. S. Campbell, B. E. de Ávila and J. Wang, Wearable biosensors for healthcare monitoring, *Nat. Biotechnol.*, 2019, **37**(4), 389–406, DOI: 10.1038/s41587-019-0045-y.

24 S. Mondal, N. Zehra, A. Choudhury and P. K. Iyer, Wearable sensing devices for point of care diagnostics, *ACS Appl. Bio Mater.*, 2020, **4**(1), 47–70, DOI: 10.1021/acsabm.0c00798.

25 S. Kadian, P. Kumari, S. Shukla and R. Narayan, Recent advancements in machine learning enabled portable and wearable biosensors, *Talanta Open*, 2023, **8**, 100267.

26 S. K. Pandit, K. Yadav, P. Chauhan and A. Kumar, Development of facile superhydrophobic coating on rockwool for oil–water separation, *Surf. Interfaces*, 2023, **39**, 102962, DOI: 10.1016/j.surfin.2023.102962.

27 P. K. Jani, K. Yadav, M. Derkaloustian, H. Koerner, C. Dhong, S. A. Khan and L. C. Hsiao, Compressing slippery surface-assembled amphiphiles for tunable haptic energy harvesters, *Sci. Adv.*, 2025, **11**(3), eadr4088, DOI: 10.1126/sciadv.adr4088.

28 U. Heredia Rivera, S. Kadian, S. Nejati, J. White, S. Sedaghat, Z. Mutlu and R. Rahimi, Printed low-cost PEDOT: PSS/PVA polymer composite for radiation sterilization monitoring, *ACS Sens.*, 2022, **7**(4), 960–971.

29 S. Kadian, N. Chaulagain, H. Rajashekhar, D. Vrushabendrakumar, G. Manik and K. Shankar, An ultra-sensitive fluorescent paper based acidic gas sensing platform. In 2021 IEEE Sensors 2021 Oct 31 (pp. 1–4). IEEE.

30 R. K. Talreja, H. Sable, V. Chaudhary, S. Kadian, M. Singh, M. Kumar, J. Kishore, V. Chaudhary and A. Khosla, Challenges in Lab-to-Clinic translation of 5th/6th generation intelligent nanomaterial-enabled biosensors, *ECS Sens. Plus*, 2024, **3**(4), 041602, DOI: 10.1149/2754-2726/ad9f7e.

31 U. Heredia-Rivera, V. Kasi, A. Krishnakumar, S. Kadian, A. K. Barui, Z. He, H. Wang, L. Stanciu and R. Rahimi, Cold atmospheric plasma-assisted direct deposition of polypyrrole-Ag nanocomposites for flexible electronic sensors, *ACS Appl. Mater. Interfaces*, 2023, **15**(13), 17078–17090.

32 U. Heredia-Rivera, S. Gopalakrishnan, S. Kadian, S. Nejati, V. Kasi and R. Rahimi, A wireless chipless printed sensor tag for real-time radiation sterilization monitoring, *J. Mater. Chem. C*, 2022, **10**(26), 9813–9822, DOI: 10.1039/d2tc00531j.

33 S. Kadian, A. Kalkal, V. Jain, S. Shukla and R. J. Narayan, Pomegranate leaf extract-based carbon dots for the selective detection of 2, 4, 6-trinitrophenol, *MRS Commun.*, 2023, **13**(5), 885–891, DOI: 10.1557/s43579-023-00430-6.

34 S. Shukla, N. N. Joshi, S. Kadian, S. S. Sahoo and R. J. Narayan, Mixed metal conductive MOFs constructed from Trypan blue linked metal nodes: characteristic features and electrochemical performance, *J. Mater. Chem. C*, 2025, **13**(8), 3886–3901, DOI: 10.1039/d4tc03867c.

35 A. Krishnakumar, S. Kadian, U. Heredia Rivera, S. Chittiboyina, S. A. Lelièvre and R. Rahimi, Organ-on-a-

chip platform with an integrated screen-printed electrode array for real-time monitoring trans-epithelial barrier and bubble formation, *ACS Biomater. Sci. Eng.*, 2023, **9**(3), 1620–1628, DOI: 10.1021/acsbiomaterials.2c00494.

36 P. Dardano, I. Rea and L. De Stefano, Microneedles-based electrochemical sensors: New tools for advanced biosensing, *Curr. Opin. Electrochem.*, 2019, **17**, 121–127, DOI: 10.1016/j.coelec.2019.05.012.

37 S. Kadian, P. Kumari, S. S. Sahoo, S. Shukla and R. J. Narayan, Machine learning enabled microneedle-based colorimetric pH sensing patch for wound health monitoring and meat spoilage detection, *Microchem. J.*, 2024, **200**, 110350.

38 A. Zareei, V. Selvamani, S. Gopalakrishnan, S. Kadian, M. K. Maruthamuthu, Z. He, J. Nguyen, H. Wang and R. Rahimi, A Biodegradable Hybrid Micro/Nano Conductive Zinc Paste for Paper-Based Flexible Bioelectronics, *Adv. Mater. Technol.*, 2022, **7**(10), 2101722, DOI: 10.1002/admt.202101722.

39 S. A. Machekposhti, S. Kadian, L. Vanderwal, S. Stafslien and R. J. Narayan, Novel hollow biodegradable microneedle for amphotericin B delivery, *MedComm*, 2023, **4**(4), e321, DOI: 10.1002/mco2.321.

40 S. Kadian, S. S. Sahoo, P. Kumari, S. Shukla and R. J. Narayan, Minimally invasive detection of buprenorphine using a carbon-coated 3D-printed microneedle array, *Microchim. Acta*, 2024, **191**(11), 672.

41 S. Kadian, G. Manik, N. Das and P. Roy, Targeted bioimaging and sensing of folate receptor-positive cancer cells using folic acid-conjugated sulfur-doped graphene quantum dots, *Microchim. Acta*, 2020, **187**(8), 458, DOI: 10.1007/s00604-020-04448-8.

42 Y. Zheng, R. Omar, R. Zhang, N. Tang, M. Khatib, Q. Xu, Y. Milyutin, W. Saliba, Y. Y. Broza, W. Wu and M. Yuan, A wearable microneedle-based extended gate transistor for real-time detection of sodium in interstitial fluids, *Adv. Mater.*, 2022, **34**(10), 2108607, DOI: 10.1002/adma.202108607.

43 S. Kadian, S. S. Sahoo, S. Shukla and R. J. Narayan, Development of 3D-printed conducting microneedle-based electrochemical point-of-care device for transdermal sensing of chlorpromazine, *J. Mater. Chem. B*, 2025, **13**(6), 2114–2123, DOI: 10.1039/d4tb01808g.

44 S. Shukla, S. A. Machekposhti, N. Joshi, P. Joshi and R. J. Narayan, Microneedle-Integrated Device for Transdermal Sampling and Analyses of Targeted Biomarkers, *Small Sci.*, 2023, **3**(6), 2200087, DOI: 10.1002/smsc.202200087.

45 T. Bedir, S. Kadian, S. Shukla, O. Gunduz and R. Narayan, Additive manufacturing of microneedles for sensing and drug delivery, *Expert Opin. Drug Delivery*, 2024, **21**(7), 1053–1068.

46 M. Parrilla, N. Claes, C. Toyos-Rodríguez, C. E. Dricot, A. Steijlen, S. Lebeer, S. Bals and K. De Wael, Wearable 3D-printed solid microneedle voltammetric sensors based on nanostructured gold for uric acid monitoring, *Biosens. Bioelectron.*, 2025, 117934, DOI: 10.1016/j.bios.2025.117934.

47 M. Parrilla, A. Sena-Torralba, A. Steijlen, S. Morais, Á. Maquieira and K. De Wael, A 3D-printed hollow microneedle-based electrochemical sensing device for in situ plant health monitoring, *Biosens. Bioelectron.*, 2024, **251**, 116131, DOI: 10.1016/j.bios.2024.116131.

48 M. Parrilla, A. Steijlen, R. Kerremans, J. Jacobs, L. den Haan, J. De Vreese, Y. V. Géron, P. Clerx, R. Watts and K. De Wael, Wearable platform based on 3D-printed solid microneedle potentiometric pH sensor for plant monitoring, *Chem. Eng. J.*, 2024, **500**, 157254.

49 A. V. Mohan, J. R. Windmiller, R. K. Mishra and J. Wang, Continuous minimally-invasive alcohol monitoring using microneedle sensor arrays, *Biosens. Bioelectron.*, 2017, **91**, 574–579, DOI: 10.1016/j.bios.2017.01.016.

50 K. Y. Goud, C. Moonla, R. K. Mishra, C. Yu, R. Narayan, I. Litvan and J. Wang, Wearable electrochemical microneedle sensor for continuous monitoring of levodopa: toward Parkinson management, *ACS Sens.*, 2019, **4**(8), 2196–2204, DOI: 10.1021/acssensors.9b01127.

51 R. K. Mishra, K. Y. Goud, Z. Li, C. Moonla, M. A. Mohamed, F. Tehrani, H. Teymourian and J. Wang, Continuous opioid monitoring along with nerve agents on a wearable microneedle sensor array, *J. Am. Chem. Soc.*, 2020, **142**(13), 5991–5995, DOI: 10.1021/jacs.0c01883.

52 Z. Li, S. Kadian, R. K. Mishra, T. Huang, C. Zhou, S. Liu, Z. Wang, R. Narayan and Z. Zhu, Electrochemical detection of cholesterol in human biofluid using microneedle sensor, *J. Mater. Chem. B*, 2023, **11**(26), 6075–6081.

53 S. Kadian and G. Manik, Sulfur doped graphene quantum dots as a potential sensitive fluorescent probe for the detection of quercetin, *Food Chem.*, 2020, **317**, 126457, DOI: 10.1016/j.foodchem.2020.126457.

54 S. Kadian, S. Shukla and R. J. Narayan, Probes for non-invasive biological visualization and biosensing of cancer cells, *Appl. Phys. Rev.*, 2023, **10**(4), 041304, DOI: 10.1063/5.0166740.

55 S. Kadian, S. S. Sahoo, P. Kumari and R. J. Narayan, Machine learning enabled onsite electrochemical detection of lidocaine using a microneedle array integrated screen printed electrode, *Electrochim. Acta*, 2024, **475**, 143664.

56 P. Joshi, P. R. Riley, W. Denning, S. Shukla, N. Khosla, J. Narayan and R. Narayan, Laser-patterned carbon coatings on flexible and optically transparent plastic substrates for advanced biomedical sensing and implant applications, *J. Mater. Chem. C*, 2022, **10**(8), 2965–2975, DOI: 10.1039/d1tc05176h.

57 K. Kim and J. B. Lee, High aspect ratio tapered hollow metallic microneedle arrays with microfluidic interconnector, *Microsyst. Technol.*, 2007, **13**(3), 231–235, DOI: 10.1007/s00542-006-0221-0.

58 N. Sargioti, T. J. Levingstone, E. D. O'Cearbhaill, H. O. McCarthy and N. J. Dunne, Metallic microneedles for transdermal drug delivery: applications, fabrication techniques and the effect of geometrical characteristics, *Bioengineering*, 2022, **10**(1), 24, DOI: 10.3390/bioengineering10010024.

59 A. Krishnakumar, R. K. Mishra, S. Kadian, A. Zareei, U. H. Rivera and R. Rahimi, Printed graphene-based electrochemical sensor with integrated paper microfluidics for rapid lidocaine detection in blood, *Anal. Chim. Acta*, 2022, **1229**, 340332.

60 A. C. Ferrari, Raman spectroscopy of graphene and graphite: Disorder, electron–phonon coupling, doping and nonadiabatic effects, *Solid State Commun.*, 2007, **143**(1–2), 47–57, DOI: 10.1016/j.ssc.2007.03.052.

61 J. Lin, Z. Peng, Y. Liu, F. Ruiz-Zepeda, R. Ye, E. L. Samuel, M. J. Yacaman, B. I. Yakobson and J. M. Tour, Laser-induced porous graphene films from commercial polymers, *Nat. Commun.*, 2014, **5**(1), 5714, DOI: 10.1038/ncomms6714.

62 A. R. Cardoso, A. C. Marques, L. Santos, A. F. Carvalho, F. M. Costa, R. Martins, M. G. Sales and E. Fortunato, Molecularly-imprinted chloramphenicol sensor with laser-induced graphene electrodes, *Biosens. Bioelectron.*, 2019, **124**, 167–175, DOI: 10.1016/j.bios.2018.10.015.

63 M. Scherf-Clavel, P. Baumann, X. M. Hart, H. Schneider, G. Schoretsanitis, W. Steimer, G. Zernig and G. Zurek, Behind the curtain: therapeutic drug monitoring of psychotropic drugs from a laboratory analytical perspective, *Ther. Drug Monit.*, 2024, **46**(2), 143–154, DOI: 10.1097/FTD.0000000000001092.

64 K. Wesner, C. Hiemke, N. Bergemann, K. M. Egberts, S. Fekete, M. Gerlach, U. Havemann-Reinecke, X. M. Lense, T. G. Riemer, G. Schoretsanitis and M. Uhr, Therapeutic reference range for olanzapine in schizophrenia: systematic review on blood concentrations, clinical effects, and dopamine receptor occupancy, *J. Clin. Psychiatry*, 2023, **84**(5), 47964, DOI: 10.4088/JCP.22r14626.

65 L. T. Rao, C. K. Mandal and F. Patolsky, Body Biofluids for Minimally-Invasive Diagnostics: Insights, Challenges, Emerging Technologies, and Clinical Potential, *Adv. Healthcare Mater.*, 2025, e03096, DOI: 10.1002/adhm.202503096.